Journal of Ultrafine Grained and Nanostructured Materials
https://jufgnsm.ut.ac.ir
Vol. 59, No.1, June 2026, pp. 90-103
Print ISSN: 2423-6845 Online ISSN: 2423-6837
DOI: 10.22059/jufgnsm.2026.01.07

Bandgap-Engineered $MAPb_{1-y}Sn_yI_3$ Absorbers via Pb/Sn Compositional Grading for High-Efficiency Perovskite Solar Cells

Ali Baghban Parashkouh, Ali Sadr*

School of Electrical Engineering, Iran University of Science and Technology, Tehran, 13114-16846, Iran

Recieved: 25 February 2026; Accepted: 25 April 2026

*Corresponding author, E-mail: sadr@iust.ac.ir

ABSTRACT

Compositional grading of the $MAPb_{1-y}Sn_yI_3$ absorber layers via controlled variation of the Pb/Sn ratio provides a pathway to enhance band alignment, and mitigate recombination in perovskite solar cells (PSCs). In this study, an optimized grading model for the $MAPb_{1-y}Sn_yI_3$ PSC is designed and simulated using SCAPS. Compounds with higher bandgap energies (E_g) are employed near the absorber/electron transporting layer (ABS/ETL), and hole transporting layer/absorber (HTL/ABS) interfaces to control the recombination rate. To enhance carrier generation, lower E_g materials are incorporated at the central regions of the absorber layer. By exploring y = 0, 0.5, and 1 as the grading end materials, the best model with power conversion efficiency (PCE) of 28.86% is achieved using $0.5<y<1$, and optimized grading depth of the absorber layer. This model improves the PCE of $MAPbI_3$ and $MASnI_3$ devices by around 22.7%, and 31.4%, respectively. Finally, a parabolic grading is employed to simulate the experimental transition of E_g between 1.18 eV and 1.3 eV.

Keywords: *Perovskite solar cell, Absorber material, Bandgap grading, Compositional grading.*

1. Introduction

Among the emerging photovoltaic (PV) technologies, PSCs have garnered significant attention as a promising light-harvesting material due to their low cost, simple fabrication methods, excellent absorption efficiency, low recombination rates, efficient charge transport, acceptable diffusion length, ideal and tunable bandgap within the visible spectrum, and the absence of deep traps in the absorber [1-6]. The efficiency of PSCs has increased rapidly, driven by advancements in compositions, film deposition techniques, and fabrication procedures [7]. Consequently, the record PCE of single-junction PSCs reached approximately 26.9% by the end of 2025 [8].

Facile bandgap tuning is an attractive feature of metal-halide perovskites, enabling performance and stability improvements [9-11]. A graded structure eliminates the need for current matching, owing to the absence of any recombination layer within the absorption region, offering an advantage over tandem configurations [12]. The best-performing PSCs to date are fabricated using absorber materials with bandgaps ranging from 1.48 - 1.62 eV [10]. However, a compromise always exists in PV devices, where wider bandgaps promote

voltage and limit spectral absorption, consequently diminishing the current density, which is improved by narrower bandgaps. Perovskites containing lead (Pb) are predominantly utilized due to their superior properties. Nevertheless, the toxicity of Pb presents a significant environmental concern. It has been demonstrated that incorporating environmentally benign tin (Sn) into perovskites represents one of the most promising alternatives to lead [2, 12-14].

During last decade, different researchers have studied mixed Pb/Sn alloys in PSCs. In 2018, Kapil et al. reported a PCE of 17.6%, by introducing a conduction band minimum (CBM) offset of ~0.15 eV at the interface between the absorber and ETL [15]. In another work, Xu et al. further improved the PCE of Pb/Sn PSCs to 18.03% by incorporating an ultrathin organic semiconductor as an intermediary between the HTL and Pb/Sn perovskite film. This approach caused better energy alignment at the HTL/ABS interface [16]. In another research, Cao et al. found a Pb/Sn gradient after antisolvent treatment, tuned by the antisolvent temperature. It enhanced charge separation and lowered carrier recombination, leading to a PCE of 22% [17]. Notably, Liu et al. introduced indium ions (In^{3+}) into perovskite solution, leading to enhanced film quality and balanced Pb/Sn ratio on the surface. As a result, accelerated charge transfer and reduced the recombination rate contributed to a PCE of 23.34% [18].

Different simulation works have studied Pb/Sn devices, looking for an optimized alternative for Pb-containing PSCs and exploring various parameters such as absorber layer thickness, defect density, doping concentration, electron affinity (EA), and materials for the ETL and HTL [19-23]. In 2024 Sadullah et al. carried out a simulation study, and tuned the bandgap of the FTO/TiO_2/$MAPb_{1-y}Sn_yI_3$/Cu_2O/anode PSC. After optimizations on thickness, defects density, energy levels of the perovskite layer, and doping density of ETL and HTL, they achieved the best PCE of 30.66% for y = 0.9 [24]. In another simulation study, Luo et al. proposed a vertical gradient in the absorber layer to address the issue of non-uniform Pb/Sn ratios across the film. After structural optimizations, their device yielded a PCE of 24.84% [25].

Although the Pb/Sn mixed PSCs have developed and achieved an experimental PCE as high as 23.7% [26], they still need to be investigated to optimize the ratio of Pb:Sn, and find more efficient configuration in ABX_3 structures [27-29]. Besides, energy band alignment is required to address the band mismatch at the interfaces of these devices [30]. Herein, the SCAPS simulation software is employed to model a graded $MAPb_{1-y}Sn_yI_3$ solar cell to achieve optimal bandgap and improved PV performance. To our knowledge, any work has systematically optimized $MAPb_{1-y}Sn_yI_3$ PSCs via three-end material bandgap grading, utilizing experimental data in numerical simulations.

2. Device Modeling and Simulation Parameters

The bandgap of mixed $MAPb_{1-y}Sn_yI_3$ perovskites is tuned from around 1.3 eV for $MASnI_3$ to approximately 1.55 eV for $MAPbI_3$. However, bandgap variation in $MAPb_{1-y}Sn_yI_3$ alloys doesn't follow Vegard's law, instead exhibiting a downshift to approximately 1.15 eV for $Sn_{0.8}Pb_{0.2}$ [9]. Importantly, different bandgaps have been reported for same composition values. Therefore, an assumption regarding the bandgap trend is necessary to simulate compositional grading in mixed Pb/Sn perovskites. In this work, experimental bandgaps for different composition values of $MAPb_{1-y}Sn_yI_3$ was collected, which are presented in Fig. 1 (a) [12, 27, 31-38]. Accurate simulation of bandgap graded devices required precise input of band energy parameters. Thus, the variation trend of E_g and EA across different composition values of $MAPb_{1-y}Sn_yI_3$ ($0 \le y \le 1$) was critical for reliably modeling the grading profile. Using the experimental data from Fig. 1 (a), a linear trend in two parts was assumed for both E_g and EA over the composition range: from y = 0 to 0.5, and y = 0.5 to 1. Although incorporating this linear trend reduced the accuracy of finding exact E_g and EA values, it brought a reasonable simplicity with an acceptable approximation for numerical simulations. In the simulations, $MAPbI_3$, $MAPb_{0.5}Sn_{0.5}I_3$, and $MASnI_3$ were selected as the end materials for compositional grading. Fig. 1 (b) and (c), and Equations (1) and (2) explain the assumed linear dependencies of E_g and EA in $MAPb_{1-y}Sn_yI_3$ alloys.

$$E_g(y) = \begin{cases} -0.74y + 1.55\ eV, & 0 \le y \le 0.5 \\ 0.24y + 1.06\ eV, & 0.5 \le y \le 1 \end{cases} \quad (1)$$

$$EA(y) = \begin{cases} 1.08y + 3.9\ eV, & 0 \le y \le 0.5 \\ -0.54y + 4.71\ eV, & 0.5 \le y \le 1 \end{cases} \quad (2)$$

An essential parameter in the numerical simulation of thin film solar cells is the thickness of the absorber layer. It has been observed that the PCE increases with absorber thickness up to a certain threshold, beyond which it saturates and eventually begins to decline [39]. Thicker absorber layers enhance the generation of photocarriers, particularly for longer wavelengths of light. However, this benefit is counterbalanced by a reduced internal electric field, and an increased recombination rate, which together contribute to a decrease in current density. On the contrary, less thickness reduces the generation current due to

limited light absorption, and the proximity of the depletion region to the contacts leads to elevated surface recombination losses [5, 40]. Therefore, an optimized thickness is required to balance these effects and ensure maximum absorption of the incident light. According to the literature, the PCE saturation point for organic metal-halide perovskites typically occurs at approximately 600 nm, beyond which no significant improvement in efficiency is observed [1, 2, 5, 39, 40].

The other essential input for device simulation is the defect properties of each layer. The main source of defects in thin film absorbers is the doping process, which directly influences the performance of the device. Thus, to obtain more accurate results in simulations, defining the defect density (N_t) for all layers is essential. In this study, the defects were neutral type with a Gaussian energetic distribution [41, 42]. The N_t were assumed to be 10^{12} cm^{-3} for $MAPbI_3$, 10^{15} cm^{-3} for $MASnI_3$, 10^{13} cm^{-3} for mixed perovskites, and 10^{15} cm^{-3} for other layers of the solar cell [13, 40, 43]. The capture cross section of electrons (σ_n) and holes (σ_p) for the $MASnI_3$ layer were set 10^{-16} and 10^{-14} cm^{-2}, respectively. For $MAPbI_3$ layer, both σ_n and σ_p were assumed to be 10^{-13} cm^{-2}, while for other layers of the device these values were set 10^{-15} cm^{-2} [40, 44]. The assumed defects properties were reliable and reasonable values utilized for all models, which might be differently reported in other literatures. The absorption coefficient (α) of each layer was defined by the SCAPS model, which depends on the E_g of the corresponding layer, as follows:

$$\alpha(\lambda) = (A + \frac{B}{h\nu})\sqrt{h\nu - E_g} \quad (3)$$

where E_g is the bandgap of the layer, hυ is the energy of the incident photon, and two absorption parameters, A (in $cm^{-1}eV^{-1/2}$) and B (in $cm^{-1}eV^{+1/2}$), are commonly set 1.00E+5 and 1.00E-12, respectively [45, 46]. This absorption model neglects sub-bandgap absorption and the Urbach tail effect.

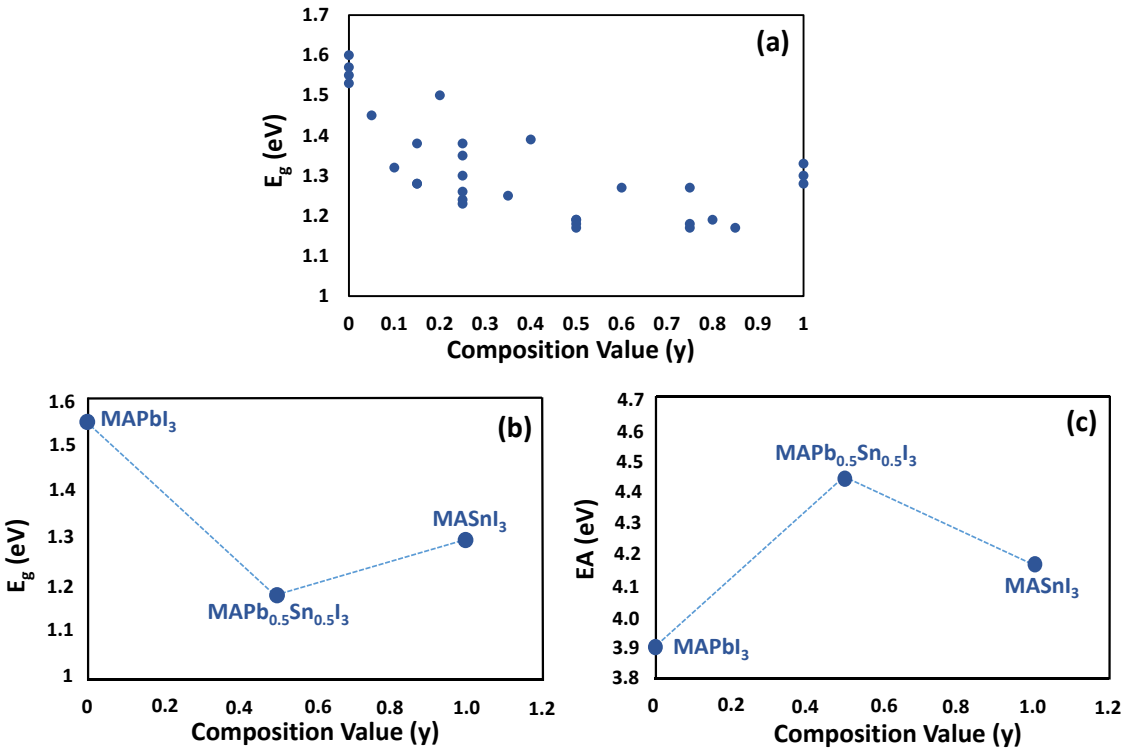

Fig. 1- (a) Bandgap variation of $MAPb_{1-y}Sn_yI_3$ alloys with different composition values (y). Assumed (b) bandgap, and (c) electron affinity trend with composition value y.

Proper selection of HTL and ETL materials is very important to determine the output characteristics of PSCs, including PCE and long-term stability [13]. PEDOT:PSS is commonly used as HTL, and can be deposited onto flexible substrates. Furthermore, solvents typically used to modify PEDOT:PSS are the same as those used in perovskite preparation, ensuring that the transport properties and conductivity of the HTL are not adversely affected [5, 47]. On the other side, PCBM is frequently employed as ETL in PSCs, which can be found in n-type, p-type, or intrinsic forms. It has been demonstrated that incorporating PCBM helps passivate charge traps within the perovskite layer during thermal annealing, thereby effectively suppresses ion migration. Consequently, the current density-voltage (J-V) hysteresis is significantly reduced or even eliminated [48, 49].

The transparent conductive oxide (TCO) layer acts as a barrier to prevent direct contact between the front electrode and the absorber layer, consequently preserving optimal device functionality [50]. The TCO of the simulated model was fluorine-doped tin oxide (FTO or SnO_2:F), while gold (Au), with a work function of 5.1 eV, was selected as the back contact material [51]. The proposed device structure, and energy levels of the selected materials are presented in Fig. 2 (a) and (b), respectively. The thickness of FTO, PCBM, and PEDOT:PSS were set 500 nm, 50 nm, and 100 nm, respectively, based on commonly reported and experimentally-validated values [1, 5, 51-53]. The FTO layer was considered as the front contact, and the flat band mode was selected in the simulations. The input parameters used for the solar cell simulations are provided in Table 1. Simulations were carried out under the standard AM1.5G solar illumination and a constant temperature of 300 K. Additionally, the series and the shunt resistance of the device were set 3 and 1000 $\Omega.cm^2$, respectively [4, 45].

Regarding the tunable bandgap of the Pb/Sn perovskite alloys, several grading models were investigated. The graded structures were specifically designed to simultaneously preserve a high open-circuit voltage (V_{OC}), and enhance the short-circuit current density (J_{SC}). By employing bandgap grading within the absorber layer, it was aimed to incorporate regions with higher bandgaps for recombination suppressing, and regions with lower bandgaps to promote light absorption. It should be noted that, the V_{OC} and J_{SC} depend on the bandgap of the space charge region, and the dominant bandgap minimum of the absorber layer, respectively [55].

Owing to the abnormal bandgap behavior of $MAPb_{1-y}Sn_yI_3$ alloys, the absorber layer in the graded models were consisted of three end materials: 1.55 eV for $MAPbI_3$, 1.3 eV for $MASnI_3$, and 1.18 eV for $MAPb_{0.5}Sn_{0.5}I_3$. During simulations, some input parameters of the $Sn_{0.5}Pb_{0.5}$ alloy were obtained via linear interpolation between the corresponding properties of two end materials. Each graded layer was assumed as binary alloy in the form of $A_{1-y}B_y$. After defining pure A, pure B, and the desired model for the compositional grading over the thickness, the specified properties of the layer, P[y(x)], were available to be extracted by the position-dependent composition value, y(x). According to the assumed trends of the E_g and EA for the $MAPb_{1-y}Sn_yI_3$ compounds (Fig. 1), a linear grading model was implemented in the simulations. The corresponding expression for the linear dependance of the bandgap on the composition value, y(x), is provided as follows:

$$\text{Linear: } E_g[y(x)] = \frac{E_{gA} \times (y_B - y(x)) + E_{gB} \times (y(x) - y_A)}{y_B - y_A} \quad (4)$$

where $E_g[y(x)]$ is the composition-dependent bandgap of the layer, y(x) is the function of the composition value along the x-direction, and E_{gA}, y_A, E_{gB}, and y_B are the bandgap and composition values for pure A and pure B materials, respectively [46].

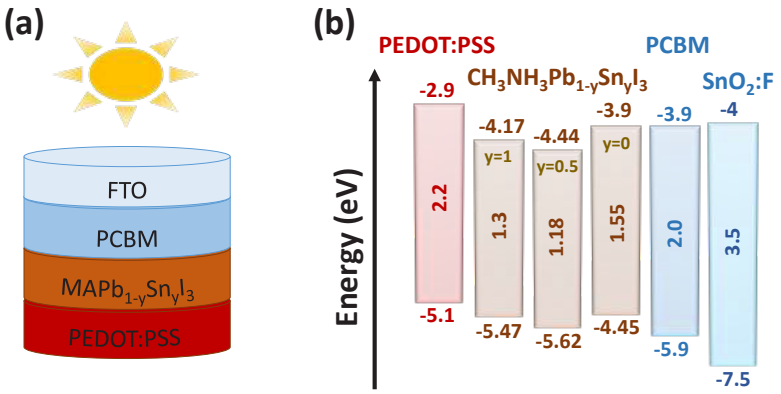

Fig. 2- (a) Proposed structure, and (b) energy levels of the simulated PSC.

Table 1- Simulation input parameters

Term	Parameter	PEDOT:PSS	PCBM	FTO	$MASnI_3$	$MAPbI_3$	$MASn_{0.5}Pb_{0.5}I_3$
Thickness	T (nm)	100	50	500	600	600	600
Bandgap	E_g (eV)	2.2	2.0	3.5	1.3	1.55	1.18
Electron Affinity	χ (eV)	2.9	3.9	4.0	4.17	3.9	4.44
Permittivity	ε_r (relative)	3	3.9	9.0	10	10	10
Effective density of states at CB	N_c ($1/cm^3$)	2.2E+15	2E+21	2.2E+17	1E+18	2.25E+18	1.6E+18
Effective density of states at VB	N_v ($1/cm^3$)	1.8E+18	2E+21	2.2E+16	1E+18	1E+18	1E+18
Thermal velocity of electrons	$V_{th,e}$ (cm/s)	1E+7	1E+7	1E+7	1E+7	1E+7	1E+7
Thermal velocity of holes	$V_{th,h}$ (cm/s)	1E+7	1E+7	1E+7	1E+7	1E+7	1E+7
Mobility of electrons	μ_n (cm^2/Vs)	1E-2	2E-1	2E+1	1.6E+0	2.2E+0	1.9E+0
Mobility of holes	μ_p (cm^2/Vs)	2E-4	2E-1	1E+1	1.6E+0	2.2E+0	1.9E+0
Acceptor density	N_a ($1/cm^3$)	1E+18	0E+0	0E+0	1E+16	1E+16	1E+16
Donor density	N_d ($1/cm^3$)	1E+10	2.93E+17	1E+15	0E+0	0E+0	0E+0
References		[5]	[51]	[5, 10, 54]	[2, 40]	[31, 40, 54]	[31, 37, 38]

3. Results and Discussion

Using data provided in Table 1, eight distinct models were examined. The initial simulations involved applying uniform bandgaps for the Pb-based ($MAPbI_3$) and Sn-based ($MASnI_3$) perovskites. In these models, the entire absorber thickness was kept at the constant bandgaps of 1.55 and 1.3 eV for the Pb-based and Sn-based models, respectively. For the graded models, the total 600 nm thickness of the absorber layer was divided into three regions. The two outer parts, adjacent to the HTL (HTL/ABS) and ETL (ABS/ETL), featured higher bandgaps than the inner parts. In the preliminary simulations, a thickness of 100 nm was assigned to the HTL/ABS and the ABS/ETL regions, while the remaining 400 nm was allocated to the central region.

Three profiles termed In-lin, with uniform absorber corners bandgap of 1.55 eV or 1.3 eV, and the absorber inner bandgaps of 1.3 eV or 1.18 eV were assessed (Fig. 3 (a)). For the In-lin models, a linear grading profile was applied to the composition value across the absorber thickness. Considering the In-lin 1.3-1.55 eV model, using the trend plotted in Fig. 2, the left half of E_g and EA ($0 \le y \le 0.5$) were used in the simulations. The inner 400 nm of the absorber was divided into two 200 nm sections, with opposing gradients directed toward the respective carrier transport layers. Lastly, the In-uni models were simulated with their absorber layer split into three uniform sections (Fig. 3 (b)). The simulation results are summarized in Table 2, including the generated power at the maximum power point (P_{MPP}) assuming a 1×1 cm^2 solar cell. Fig. 3 (c-e) illustrate the J-V, power density-voltage (P-V), and external quantum efficiency (EQE) curves of the eight simulated models, respectively.

As shown in Table 2 and Fig. 3 (c) and (d), the highest PCE was achieved by the In-uni profile within the bandgap range of 1.18-1.3 eV, outperforming the next high-performance model by approximately 1.4%. Also, the In-uni 1.18-1.3 eV model yielded the best J_{SC} of 36.86 mA/cm^2, while maintaining acceptable values for FF and V_{OC} at 65.14% and 1.04 V, respectively. The considerable PCE of 25.00% demonstrated the potential of bandgap compositional engineering to enhance device performance, which was further confirmed

by its EQE spectra, as shown in Fig. 3 (e). This enhancement suggested that further optimization could lead to additional improvements. Sorting by PCE, the second and third models were In-lin 1.18-1.3 eV, and uniform Pb-based, with the PCE values of 23.63% and 23.51%, respectively. Although their PCE values were almost similar, differences were observed in their V_{OC} and J_{SC}. The uniform Pb-based model exhibited a remarkable V_{OC} of 1.27 V, highlighting the influence of the absorber layer's bandgap on the device voltage. In contrast, the 34.89 mA/cm^2 current density of the In-uni 1.18-1.3 eV model showed the key role of lower bandgaps in the generation processes.

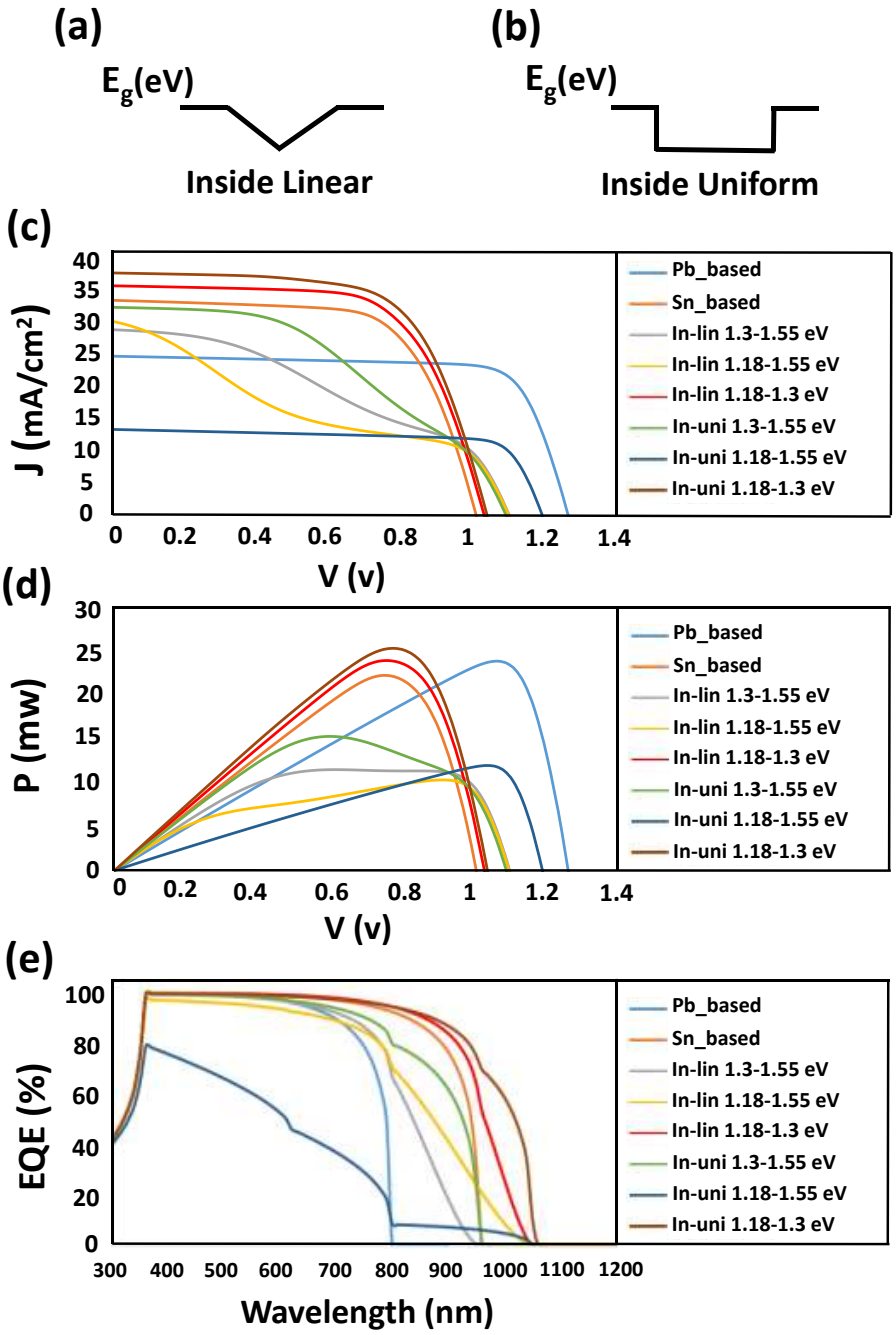

Fig. 3- The assessed models for bandgap simulation: (a) Inside linear, and (b) Inside uniform. The simulation results as: (c) J-V, (d) P-V, and (e) EQE curves.

Table 2- Simulation results of the perovskite graded profiles

Model	PCE (%)	FF (%)	J_{SC} (mA/cm^2)	V_{OC} (V)	J_{MPP} (mA/cm^2)	V_{MPP} (V)	P_{MPP} (mW)
Uniform Pb-based	23.51	76.70	24.18	1.27	22.03	1.07	23.57
Uniform Sn-based	21.96	66.40	32.70	1.01	29.13	0.75	21.85
In-lin 1.3-1.55 eV	11.34	36.43	28.21	1.10	18.41	0.62	11.41
In-lin 1.18-1.55 eV	10.15	31.30	29.46	1.10	11.10	0.91	10.10
In-lin 1.18-1.3 eV	23.63	65.53	34.89	1.03	31.12	0.76	23.65
In-uni 1.3-1.55 eV	15.10	43.6	31.65	1.09	25.1	0.6	15.06
In-uni 1.18-1.55 eV	11.77	75.45	13.05	1.20	11.30	1.04	11.75
In-uni 1.18-1.3 eV	25.00	65.14	36.86	1.04	32.16	0.78	25.08

Both graded models in the range of 1.3-1.55 eV suffer from poor FF and J_{SC}, which resulted in their limited PCE. The FF suppression could be attributed to the holes back-transfer toward ETL. Compared to 1.18 eV case with valance band maximum (VBM) = 4.62 eV, the 1.3 eV-core absorber with VBM = 4.47 eV showed decreased resistance against this destructive phenomenon. Moreover, according to Fig. 3 (e) they exhibited reduced EQE, although it was slightly compensated in the In-uni 1.3-1.55 eV model due to better absorption caused by thicker 1.3 eV part. Similarly, both 1.18-1.55 eV models showed decreased performance. The large energy barrier formed between the CBMs of 1.18 eV and 1.55 eV layers limited the flow of electrons toward cathode. The In-lin 1.18-1.55 eV model showed better EQE in comparison with In-uni 1.18-1.55 eV, caused by the extra force form energy levels slope. Compared to In-uni 1.18-1.3 eV model, the In-lin 1.18-1.3 eV showed slightly lower J_{SC}. It was resulted from its reduced light absorption in the central regions of the perovskite layer, which caused EQE reduction in Fig. 3 (e).

To further optimize the In-uni 1.18-1.3 eV model, the grading depth near both interfaces was investigated. The effect of varying the thicknesses of the ABS/ETL and HTL/ABS parts were evaluated for the 600 nm absorber layer. To determine the optimal situation for these regions, their thickness was varied between 10 nm and 150 nm in 10 nm increments, while the opposing side was maintained at a constant thickness of 50 nm. Thus, by increasing the thickness of the outer parts, the inner part thickness was reduced. The results of the ABS/ETL and HTL/ABS optimization process are presented in Fig. 4.

Based on the simulation results, the PCE of the graded structure indicated a significant improvement after optimizations. Initially, when the thickness of the ABS/ETL part was set 20 nm, the PCE increased to the value of 27.53%. In this situation, the FF, J_{SC}, and V_{OC} were 67.7%, 37.6 mA/cm^2, and 1.08 V, respectively. Carrier generation is very important at the front side. Thus, the graded region was confined to a thinner part to allow more absorption by the 1.18 eV core. On the other hand, the wider bandgap helped to significantly control the recombination rate near the ABS/ETL interface. This enhancement was achieved by the increased and more effective electric field in the thickness optimized In-uni 1.18-1.3 eV model, as discussed later.

Afterward, optimization of the HTL/ABS part led to the highest PCE of 28.05%, achieved by the HTL/ABS thickness of 10 nm. As well, the FF, J_{SC}, and V_{OC} values were 68.8%, 37.66 mA/cm^2, and 1.08 V, respectively. However, further increase in the thickness of the 1.3 eV layers near the HTL and ETL caused a gradual decrease in the PCE. For the back interface, repelling minority electrons and controlling the recombination rate was essential. Simulation results showed that a 10 nm thick 1.3 eV part near HTL interface was sufficient to improve the PCE. Although, increasing the bandgap was beneficial for the V_{OC} and recombination controlling, a compromise was needed between the generated current and the voltage. Importantly, when bandgap widening was implemented on both sides of the absorber layer, compensation for the loss in J_{SC} was addressed within the central region of the absorber. It should be noted that, the fabrication of a graded structure in the thicknesses of around 10 nm is really challenging. Experimentally, approaches such as surface treatment [56, 57], surface doping [58], post-treatment strategies [59], additive engineering [60, 61], and etc. are often used to realize graded films and energy levels alignment in PSCs.

Using achievements in Fig. 4 (a), we simulated the optimized In-uni 1.18-1.3 eV

model, employing an absorber layer composed of three distinct regions: 10 nm, 570 nm, and 20 nm for the HTL/ABS, inner, and ABS/ETL regions, respectively. Interestingly, this internal optimization increased the PCE of the In-uni 1.18-1.3 eV to 28.86%. Notably, it exhibited the best J_{SC}, J_{MPP}, and P_{MPP} in comparison with models of Table 2, with the values of 37.78 mA/cm^2, 34.29 mA/cm^2, and 28.80 mW, respectively. Compared to the Pb-based and Sn-based uniform structures, this model enhanced the PCE by 22.7%, and 31.4%, respectively. Although, the V_{OC} and V_{MPP} of the optimized In-uni 1.18-1.3 eV model were slightly lower than those of uniform Pb-based counterpart, they remained within an acceptable range, with values of 1.1 V and 0.84 V, respectively. The J-V and EQE curves for these models are presented in Fig. 5 (a)

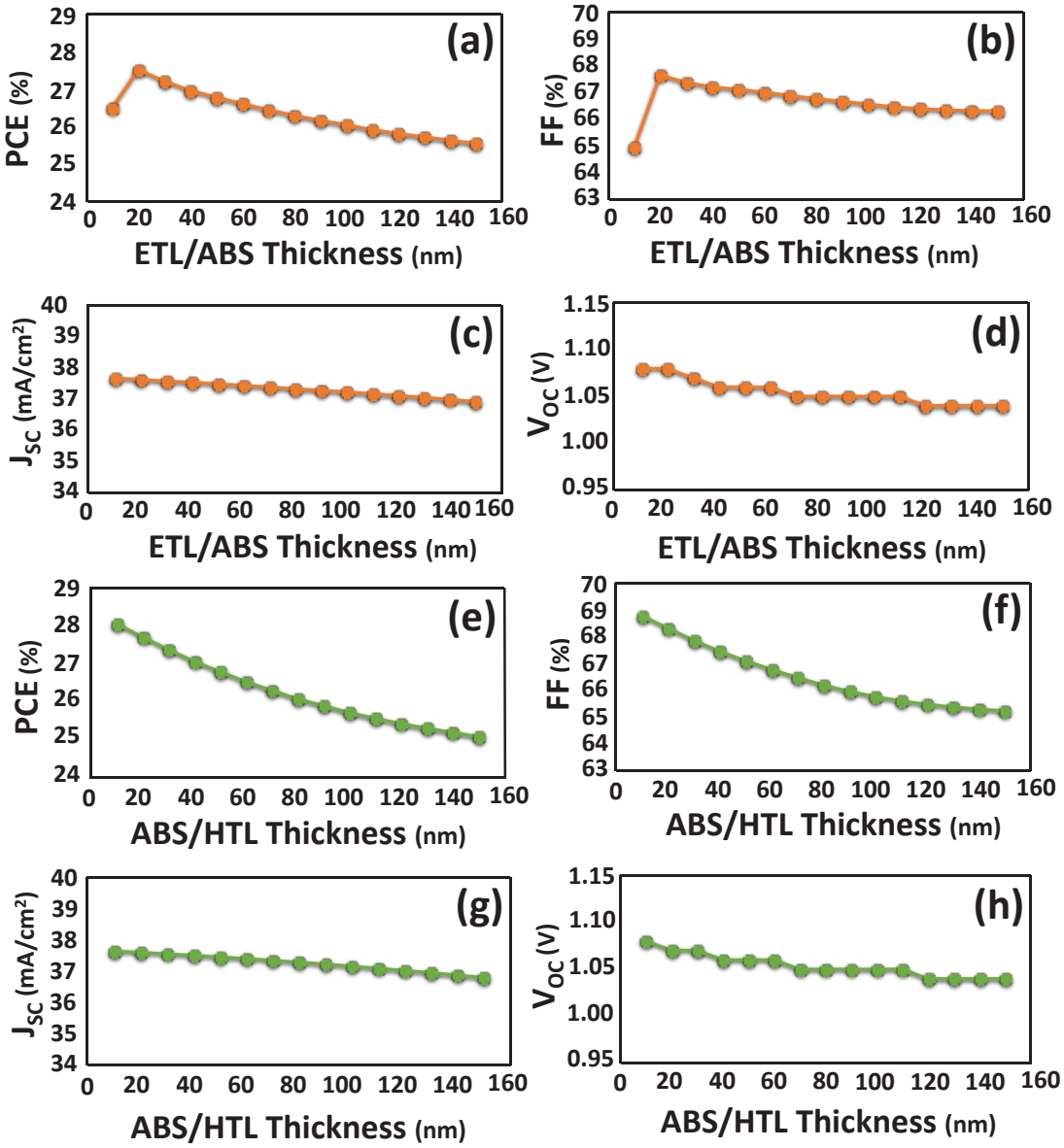

Fig. 4- ABS/ETL thickness optimization results (a) PCE, (b) FF, (c) JSC and (d) V_{OC}. HTL/ABS thickness optimization results (e) PCE, (f) FF, (g) J_{SC}, and (h) V_{OC}.

and (b), respectively. Furthermore, the bandgap dependent absorption edge was around 800 nm for Pb-based, 954 nm for Sn-based and, 1051 nm for both normal and optimized In-uni 1.18-1.3 eV models.

The recombination rate across the absorber was influenced by the bandgap and defect characteristics of each model. As illustrated in Fig. 5 (c), for the models with the absorber E_g of 1.18 eV, a spike was formed at the both HTL/ABS and ABS/ETL interfaces. It can be seen that the In-uni models exhibited higher recombination rate at interfaces. However, for the optimized In-uni 1.18-1.3 eV model the high spikes were limited to smaller regions of the absorber, leading to better V_{OC} and a marginally higher J_{SC}. In contrast, although the Pb-based model had higher recombination rate across the absorber, its relatively lower recombination rate near the interfaces contributed to its better V_{OC}, and overall performance.

As shown in Fig. 6(a-c), the applied graded structure upward shifted both VBM and CBM near HTL, but the larger amount of change in CBM formed the higher bandgap near the HTL/ABS and ABS/ETL interfaces. At the HTL/ABS side, the slope in VBM formed an extra electrical force to extract holes. For the thickness optimized In-uni 1.18-1.3 eV model, where this slope got closer to the interface at X = 100 nm, a more effective force helped to reduce the recombination rate, as showed in Fig. 5(c). Similarly on the other side, the slope of CBM caused better electrons transport, while suppressing the accumulation of holes in the vicinity of ETL. The resulted electric field is shown in Fig. 6(d-f). Near both HTL/ABS and ABS/ETL interfaces, a higher magnitude was found for the thickness optimized In-uni 1.18-1.3 eV model, which was the reason for its increased J_{SC}, and enhanced performance. At the ABS/ETL interface, the Pb_based model showed opposite direction compared to other models. It wasn't preferred, because it repelled the flow of electrons toward ETL.

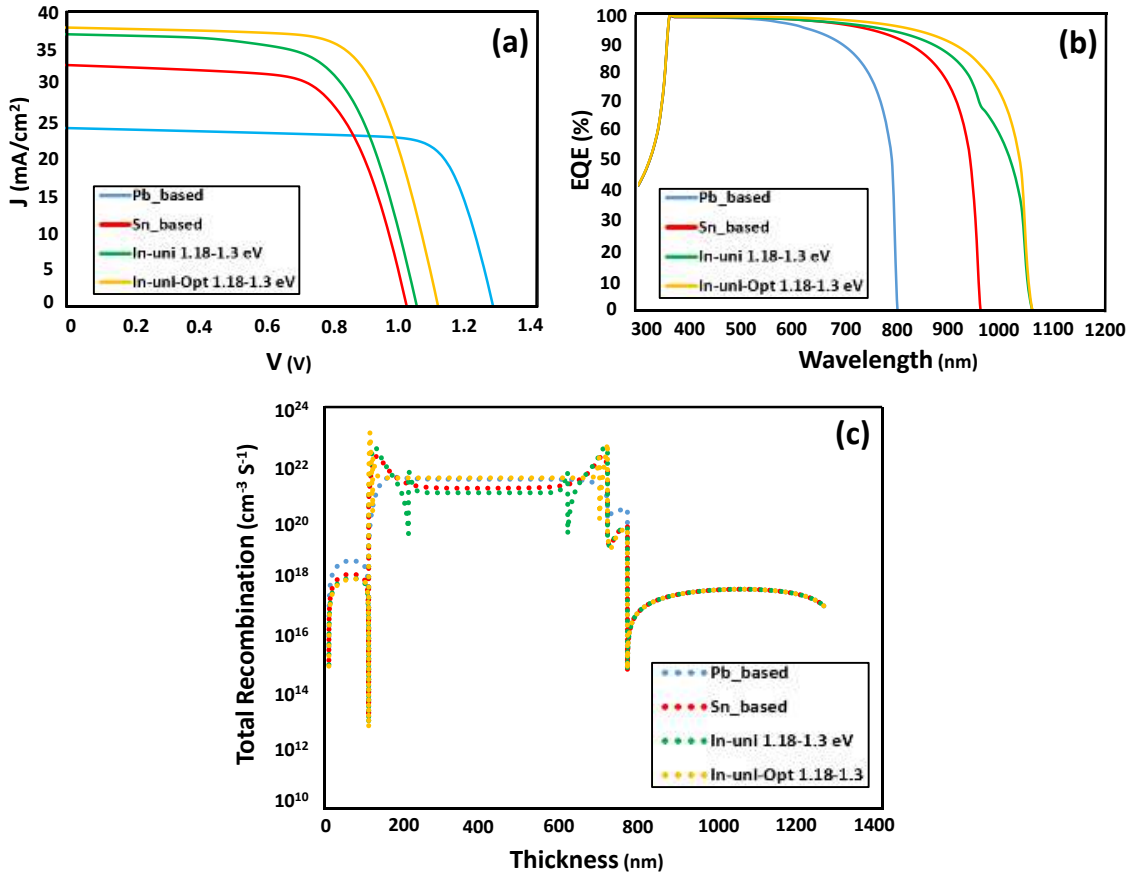

Fig. 5- (a) J-V, (b) EQE, and (c) total recombination comparison for Pb-based, Sn-based, In-uni 1.3-1.18 eV, and thickness optimized In-uni 1.18-1.3 eV models.

The other parameter studied for the graded structure, was working in high temperatures. Operating temperature has a direct influence on the quality of the absorber material in solar cells, leading to stress and strain within the material. This can result in several challenges, including distortion, disorder, and the formation of pinholes. Such challenges can result in increased density of bulk and interfacial defects. As a consequence, both the diffusion length and series resistance are adversely affected by the increased temperature, thereby weakening the overall efficiency of the solar cell [62, 63].

Different materials show different responses when exposed to temperatures exceeding 300 K. In real situation, temperature fluctuations occur due to several factors such as altitude, latitude, time of year, and the time of day, depending on working place [64]. At elevated temperatures, the increase in saturation current leads to a reduction in the V_{OC}. Besides, J_{SC} is affected by two competing factors: the ideal current, which decreases with temperature, and the enhanced carrier collection, which improves at higher temperatures. Depending on which of these factors predominates in the device, the J_{SC} may either increase or decrease with rising temperatures [65].

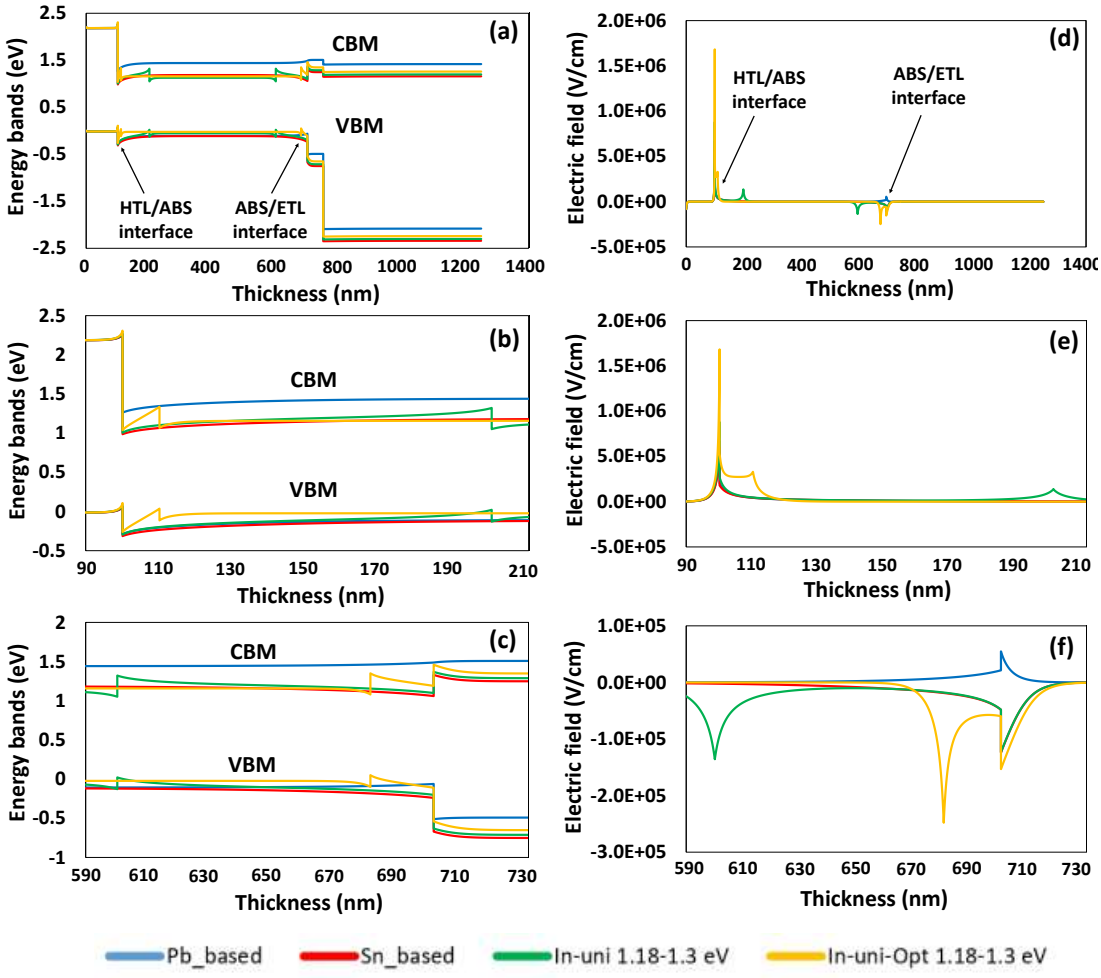

Fig. 6- Band diagrams (a-c) and electric field (d-f) comparison between Pb_based, Sn-based, In-uni 1.3-1.18 eV, and thickness optimized In-uni 1.18-1.3 eV models: (a,d) across the complete thickness, (b,e) near the HTL/ABS interface, and (c,f) near the ABS/ETL interface.

The impact of increasing temperatures on the operation Pb-based, Sn-based, In-uni 1.3-1.18 eV, and optimized In-uni 1.18-1.3 eV models were investigated via simulations. The working temperature of the simulated models was varied from 300 to 450 K. The overall behavior of all these models was found to be similar. With the exception of J_{SC}, all other PV parameters decreased by increasing the temperature, although, the controlled recombination in the optimized In-uni 1.18-1.3 eV model improved its V_{OC} stability. Fig. 7 illustrates the effect of temperature variation on the V_{OC}, J_{SC}, FF, and PCE of the selected models.

Because of the ideal E_g transition in the In-uni 1.18-1.3 eV model, and its fabrication challenges [66, 67], another model employing a parabolic grading profile with various bowing parameters (b) was introduced. The bowing parameter defined the curvature of the bandgap, and determined the distance between the inner 1.18 eV region and interfaces. To complete previous optimizations, $MAPb_{0.5}Sn_{0.5}I_3$ and $MASnI_3$ were selected as the end materials in the parabolic grading model. In this model denoted as In-para 1.18-1.3 eV, the inner 570 nm of the absorber was consisted of two parabolic outer parts with variable lengths (L_para) to shift the bandgap between 1.18 eV and 1.3 eV, as illustrated in Fig. 8 (a). by increasing the value of b, the thickness of L_para decreased, caused the bandgap profile to approach the configuration used in the In-uni models.

To investigate the effect of bowing parameters, the In-para 1.18-1.3 eV model with b=14.1 and b=1.42 was described in more detail. In these cases, the 570 nm inner region of the absorber was composed of two parabolic parts measuring 20 nm and 200 nm, respectively. The variation algorithm of y, along the inner 570 nm of the absorber, and the corresponding bandgap profiles in the device are depicted in Fig. 8 (b) and (c), respectively. Applying these two parabolic grading profiles, the PCE of the solar cell dropped to 28.04% for b=14.1, and 27.41% for b=1.42. Despite this reduction, these PCE values remained higher than those of the other models presented in Table 2. Additionally, the FF, V_{OC}, and J_{SC} of these models were 68.11%, 1.09 V, and 37.67 mA/cm^2 for b=14.1, and 68.62%, 1.08 V, and 36.69 mA/cm^2 for b=1.42. The decrease in J_{SC} in the latter model can be attributed to the smaller 1.18 eV inner section. The effect of increasing the L_para values on the PCE of the solar cell is shown in Fig. 8 (d). As expected, larger L_para values (smaller b) reduced the PCE of the device, due to the difference from the ideal bandgap transition. Finally, the J-V and P-V curves of the models are compared in Fig. 7 (e) and (f), respectively.

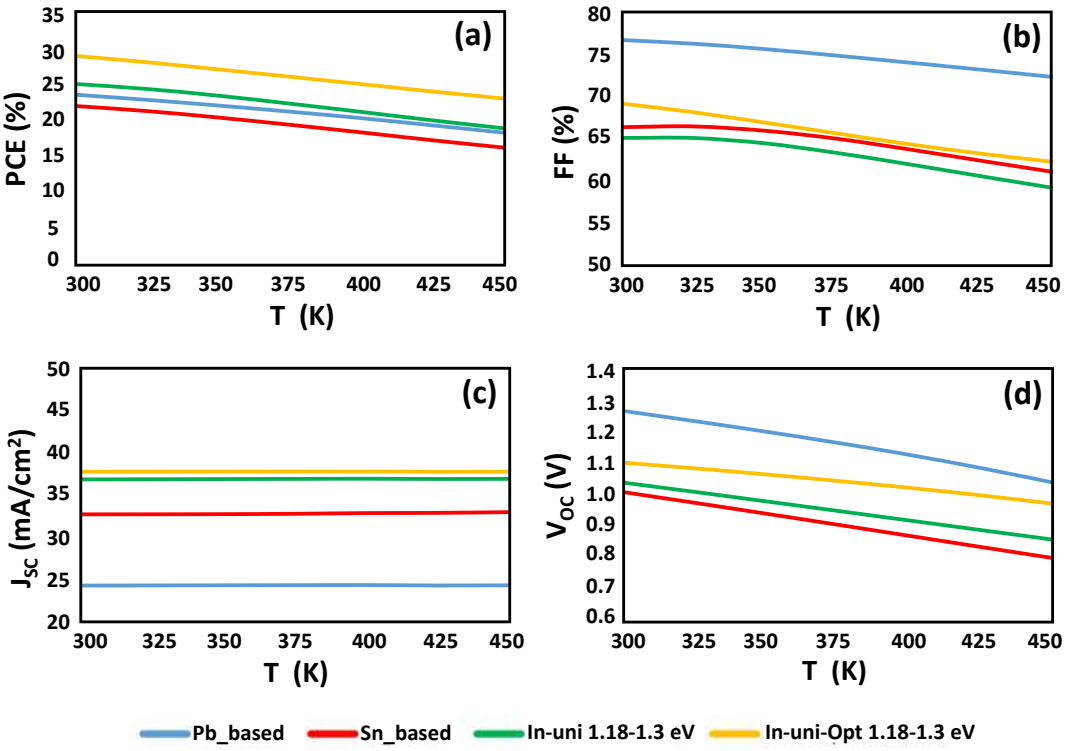

Fig. 7- The effect of operating temperature variation on (a) PCE, (b) FF, (c) J_{SC}, and (d) V_{OC} for Pb-based, Sn-based, In-uni 1.3-1.18 eV and thickness optimized In-uni1.18-1.3 eV models.

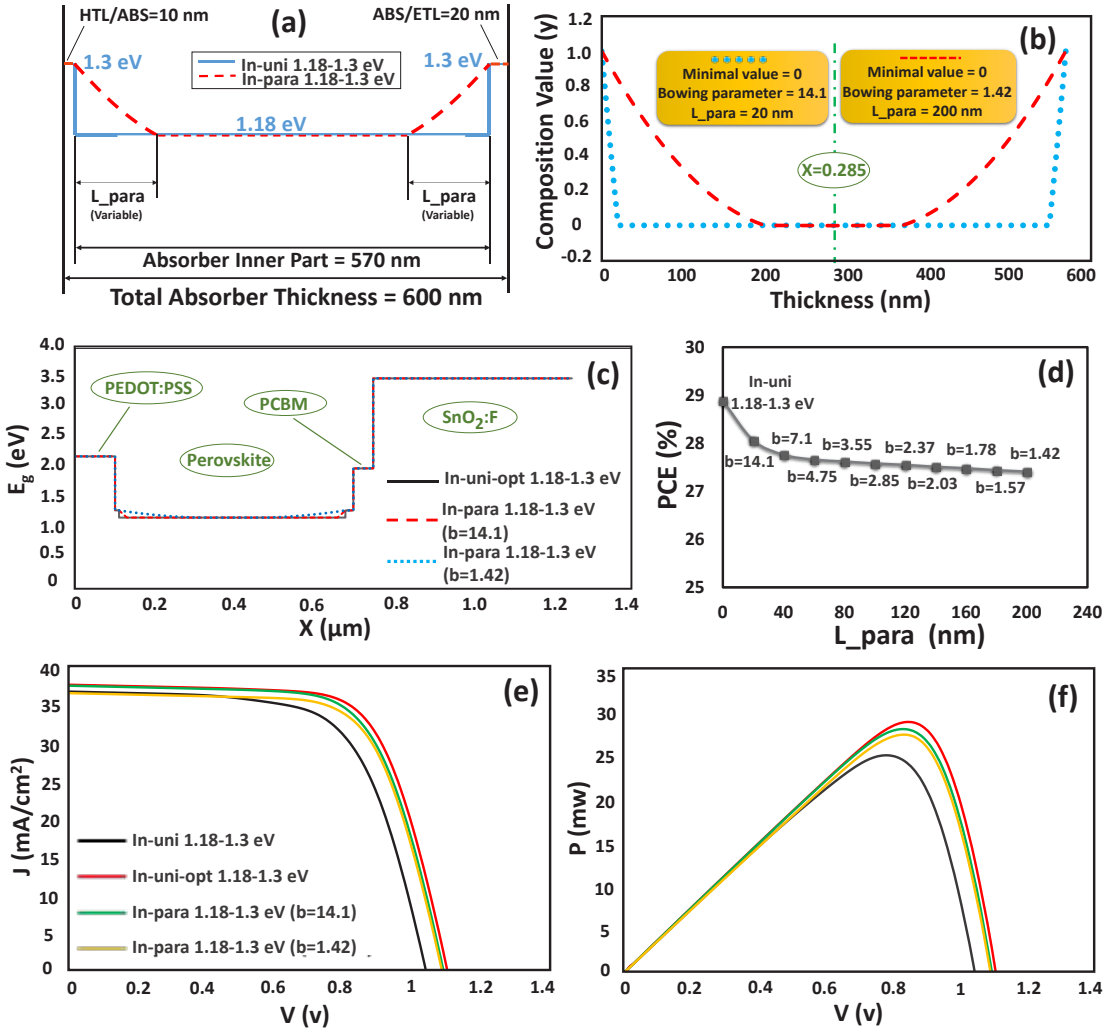

Fig. 8- (a) Schematic illustration of In-uni and In-para models. (b) Variation of the composition value for In-para models. (c) Bandgap profile for optimized In-uni and In-para 1.18-1.3 eV (b=14.1 and b=1.42) models. (d) PCE of the In-para 1.18-1.3 eV model with different L_para values. (e) J-V and (f) P-V curves of the In-uni 1.18-1.3 eV, optimized In-uni 1.18-1.3 eV and In-para 1.18-1.3 eV (b=14.1 and b=1.42) models.

According to the electrical behavior of semiconductors, an extra electric field was formed at the gradient parts of the bandgap. Depending on its direction, it could be beneficial when strengthening the built-in electric field (E_{bi}) of the device. Boosting E_{bi} increased the carrier diffusion length and accelerated carrier transport toward electrodes, thereby improved the charge separation efficiency. Moreover, the recombination rate was decreased, leading to further improvements in device performance. This phenomenon was considered in the design of the graded structure. This extra force caused by the bandgap gradient was more useful, in the regions with higher recombination rate and speed. When the bandgap increased near the ABS/HTL interface, an extra electric field was formed in the same direction with E_{bi}. As a result, carrier collection was enhanced by the improved carrier diffusion length. On the contrary, when the bandgap was decreased near the ABS/HTL interface, the carrier collection, and thus, the J_{SC} values were limited by the reverse electric field.

A similar effect was observed on the front side of the absorber layer, where the increasing bandgap formed an opposite electric field with the E_{bi}. One of the key functions of the graded structure was effectively controlling the recombination rate and generation process simultaneously. This was achieved by carefully designing the bandgap profile

to create a resultant electric field that counteracts E_{bi} in regions, where recombination needs to be suppressed. To sum up, the bandgap near two interfaces was used to enhance the recombination and V_{OC}, while the inner regions of the absorber were optimized to improve light absorption and increase J_{SC}.

4. Conclusion

In this study, a compositionally-graded $MAPb_{1-y}Sn_yI_3$ solar cell employing end materials with y=0, 0.5 and 1 was simulated using SCAPS. Several graded structures were investigated by varying the bandgap profile within the 600 nm absorber layer. After optimizations, the In-uni 1.18-1.3 eV model showed the best PCE among the graded structures. In this model, the absorber layer was divided into three uniform bandgaps of 1.3 eV (20 nm), 1.18 eV (570 nm), and 1.3 eV (10 nm), arranged from the front to the back-side of the solar cell. It increased the PCE of the simulated $MAPbI_3$ and $MASnI_3$ structures by 22.7% and 31.4%, respectively, reaching the value of 28.86%. This strategy yielded a J_{SC} of 37.78 mA/cm^2, and V_{OC} of 1.1 V. Considering practical assumptions and experimental aspects, the In-para 1.18-1.3 eV model was designed to parabolically change the bandgap between 1.18 eV and 1.3 eV. It was demonstrated that increasing the bowing parameter led to a model closer to the ideal situation with higher PCEs. It was indicated that the proposed approach can potentially enhance the performance of Pb/Sn PSCs, and warrants further study in the future simulation and fabrication researches.

Acknowledgements

The authors pay the gratitude to Prof. Marc Burgelman, University of Gent, Belgium and acknowledge him for providing SCAPS software.

References

1. Salah, M.M., et al., A comparative study of different ETMs in perovskite solar cell with inorganic copper iodide as HTM. Optik, 2019. 178: p. 958-963.
2. Mandadapu, U., et al., Design and simulation of high efficiency tin halide perovskite solar cell. International Journal of Renewable Energy Research, 2017. 7(4): p. 1603-1612.
3. Casas, G., et al., Analysis of the power conversion efficiency of perovskite solar cells with different materials as Hole-Transport Layer by numerical simulations. Superlattices and Microstructures, 2017. 107: p. 136-143.
4. Bansal, S. and P. Aryal. Evaluation of new materials for electron and hole transport layers in perovskite-based solar cells through SCAPS-1D simulations. in 2016 IEEE 43rd Photovoltaic Specialists Conference (PVSC). 2016. IEEE.
5. Mandadapu, U., S.V. Vedanayakam, and K. Thyagarajan, Simulation and analysis of lead based perovskite solar cell using SCAPS-1D. Indian Journal of Science and Technology, 2017. 10(11): p. 65-72.
6. Parashkouh, A.B., et al., Improved Lead Halide Perovskite Films and Devices Using Hot-Flow-Assisted Annealing. IEEE Journal of Photovoltaics, 2025.
7. Park, J., et al., Controlled growth of perovskite layers with volatile alkylammonium chlorides. Nature, 2023. 616(7958): p. 724-730.
8. Green, M.A., et al., Solar cell efficiency tables (version 66). Progress in Photovoltaics, 2025. 33(NREL/JA--5900-94273).
9. Gholipour, S. and M. Saliba, Bandgap tuning and compositional exchange for lead halide perovskite materials, in Characterization Techniques for Perovskite Solar Cell Materials. 2020, Elsevier. p. 1-22.
10. Prasanna, R., et al., Band gap tuning via lattice contraction and octahedral tilting in perovskite materials for photovoltaics. Journal of the American Chemical Society, 2017. 139(32): p. 11117-11124.
11. Ferrara, C., et al., Wide band-gap tuning in Sn-based hybrid perovskites through cation replacement: the FA 1– x MA x SnBr 3 mixed system. Journal of Materials Chemistry A, 2017. 5(19): p. 9391-9395.
12. Konstantakou, M. and T. Stergiopoulos, A critical review on tin halide perovskite solar cells. Journal of Materials Chemistry A, 2017. 5(23): p. 11518-11549.
13. Owolabi, J.A., et al., Investigating the Effect of ZnSe (ETM) and Cu2O (HTM) on Absorber Layer on the Performance of Pervoskite Solar Cell Using SCAPS-1D. Am J Phys Appl, 2020. 8(1): p. 1.
14. Mehra, S., et al., Evaluating Pb-based and Pb-free halide perovskites for solar-cell applications: a simulation study. Heliyon, 2024. 10(12).
15. Kapil, G., et al., Highly efficient 17.6% tin–lead mixed perovskite solar cells realized through spike structure. Nano letters, 2018. 18(6): p. 3600-3607.
16. Xu, G., et al., Integrating ultrathin bulk-heterojunction organic semiconductor intermediary for high-performance low-bandgap perovskite solar cells with low energy loss. Advanced Functional Materials, 2018. 28(42): p. 1804427.
17. Cao, J., et al., High-performance tin–lead mixed-perovskite solar cells with vertical compositional gradient. Advanced Materials, 2022. 34(6): p. 2107729.
18. Liu, H., et al., Indium Iodide Additive Realizing Efficient Mixed Sn—Pb Perovskite Solar Cells. Advanced Energy Materials, 2024. 14(17): p. 2304234.
19. Wang, A., X. Gan, and J. Yu, Simulation of narrow-bandgap mixed Pb–Sn perovskite solar cells with inverted pin structure. Optical Materials, 2021. 112: p. 110751.
20. Zhang, W., et al., Revealing key factors of efficient narrow-bandgap mixed lead-tin perovskite solar cells via numerical simulations and experiments. Nano Energy, 2022. 96: p. 107078.
21. Al Husseini, H.B. and A.M. Jafar, An analysis comparing the performance of lead and tin halides organic perovskite solar cells and numerical simulation with SCAPS. Optical Materials, 2024. 155: p. 115814.
22. Rahaman, M., et al., Numerical optimization of lead-based and lead-free absorber materials for perovskite solar cell (PSC) architectures: A SCAPS-1D simulation. AIP Advances, 2024. 14(9).
23. Moone, P.K. and N. Sharifi, Comparison of Pb-based and Sn-based perovskite solar cells using SCAPS simulation: optimal efficiency of eco-friendly CsSnI3 devices. Environmental Science and Pollution Research, 2024. 31(39): p. 51447-51460.
24. Sadullah, M. and K. Ghosh, Bandgap tuning and performance analysis of hybrid MAPb1– xSnxI3 perovskite solar cell: A numerical approach. Optik, 2024. 300: p. 171644.
25. Luo, W., et al., Optimization of vertical gradient Pb-Sn hybrid perovskite solar cells using SCAPS (Solar Cell Capacitance Simulator). Materials Today Communications, 2024. 39: p. 108894.
26. Bai, L., et al., Optimization of Sn defects through multiple coordination effect to realize stable Sn–Pb mixed perovskite solar cells. Solar Energy Materials and Solar Cells, 2023. 254: p. 112283.

27. Badrooj, M., F. Jamali-Sheini, and N. Torabi, Roles of Sn content in physical features and charge transportation mechanism of Pb-Sn binary perovskite solar cells. Solar Energy, 2020. 209: p. 590-601.
28. Badrooj, M., F. Jamali-Sheini, and N. Torabi, Zn-doped Pb/Sn hybrid perovskite solar cells: Towards high photovoltaic performance. Solar Energy, 2022. 236: p. 63-74.
29. Guli, M., et al., Effect of ABX 3 site changes on the performance of tin–lead mixed perovskite solar cells. Nanoscale, 2024. 16(37): p. 17276-17299.
30. Yin, C., et al., Numerical investigation of eco-friendly FASnI3 perovskite solar cells: Effects of energy band alignment and interface defect. Micro and Nanostructures, 2025. 203: p. 208147.
31. Hao, F., et al., Anomalous band gap behavior in mixed Sn and Pb perovskites enables broadening of absorption spectrum in solar cells. Journal of the American Chemical Society, 2014. 136(22): p. 8094-8099.
32. Anaya, M., et al., Optical analysis of CH 3 NH 3 Sn x Pb 1− x I 3 absorbers: a roadmap for perovskite-on-perovskite tandem solar cells. Journal of Materials Chemistry A, 2016. 4(29): p. 11214-11221.
33. Zhao, B., et al., High open-circuit voltages in tin-rich low-bandgap perovskite-based planar heterojunction photovoltaics. Advanced materials, 2017. 29(2): p. 1604744.
34. Yang, Z., A. Rajagopal, and A.K.Y. Jen, Ideal bandgap organic–inorganic hybrid perovskite solar cells. Advanced Materials, 2017. 29(47): p. 1704418.
35. Zhu, H.L., et al., Controllable Crystallization of CH3NH3Sn0. 25Pb0. 75I3 Perovskites for Hysteresis-Free Solar Cells with Efficiency Reaching 15.2%. Advanced Functional Materials, 2017. 27(11): p. 1605469.
36. Li, L., et al., High efficiency planar Sn–Pb binary perovskite solar cells: controlled growth of large grains via a one-step solution fabrication process. Journal of Materials Chemistry C, 2017. 5(9): p. 2360-2367.
37. Li, Y., et al., 50% Sn-Based Planar Perovskite Solar Cell with Power Conversion Efficiency up to 13.6%. Advanced Energy Materials, 2016. 6(24): p. 1601353.
38. Ogomi, Y., et al., CH3NH3Sn x Pb (1–x) I3 Perovskite solar cells covering up to 1060 nm. The journal of physical chemistry letters, 2014. 5(6): p. 1004-1011.
39. Hossain, M.F., M. Faisal, and H. Okada. Device modeling and performance analysis of perovskite solar cells based on similarity with inorganic thin film solar cells structure. in 2016 2nd International Conference on Electrical, Computer & Telecommunication Engineering (ICECTE). 2016. IEEE.
40. Anwar, F., et al., Effect of different HTM layers and electrical parameters on ZnO nanorod-based lead-free perovskite solar cell for high-efficiency performance. International Journal of Photoenergy, 2017. 2017.
41. Minemoto, T. and M. Murata, Theoretical analysis on effect of band offsets in perovskite solar cells. Solar Energy Materials and Solar Cells, 2015. 133: p. 8-14.
42. Samiee, M., et al., Defect density and dielectric constant in perovskite solar cells. Applied Physics Letters, 2014. 105(15).
43. Lenka, T., et al., Numerical analysis of high-efficiency lead-free perovskite solar cell with NiO as hole transport material and PCBM as electron transport material. CSI Transactions on ICT, 2020. 8: p. 111-116.
44. Somay, S., A. Kumar, and S.K. Pandey, Design perspective and numerical analysis of all perovskite 2-terminal and 4-terminal tandem solar cell. Micro and Nanostructures, 2022. 167: p. 207240.
45. Karthick, S., S. Velumani, and J. Bouclé, Experimental and SCAPS simulated formamidinium perovskite solar cells: A comparison of device performance. Solar Energy, 2020. 205: p. 349-357.
46. Burgelman, M., et al., SCAPS manual. 2016, February.
47. Wu, D.T., et al., Enhancing the Efficiency and Stability of Tin-Lead Perovskite Solar Cells via Sodium Hydroxide Dedoping of PEDOT: PSS. Small Methods, 2024. 8(12): p. 2400302.
48. Yang, D., et al., Stable efficiency exceeding 20.6% for inverted perovskite solar cells through polymer-optimized PCBM electron-transport layers. Nano letters, 2019. 19(5): p. 3313-3320.
49. Zhong, Y., et al., Role of PCBM in the Suppression of Hysteresis in Perovskite Solar Cells. Advanced Functional Materials, 2020: p. 1908920.
50. Fahsyar, P.N.A., et al., Correlation of simulation and experiment for perovskite solar cells with MoS2 hybrid-HTL structure. Applied Physics A, 2021. 127(5): p. 1-10.
51. Azri, F., et al., Electron and hole transport layers optimization by numerical simulation of a perovskite solar cell. Solar energy, 2019. 181: p. 372-378.
52. Haider, S.Z., H. Anwar, and M. Wang, A comprehensive device modelling of perovskite solar cell with inorganic copper iodide as hole transport material. Semiconductor Science and Technology, 2018. 33(3): p. 035001.
53. Lin, L., et al., Modeling and analysis of HTM-free perovskite solar cells based on ZnO electron transport layer. Superlattices and Microstructures, 2017. 104: p. 167-177.
54. Husainat, A., et al., Simulation and analysis of methylammonium lead iodide (CH3NH3PbI3) perovskite solar cell with Au contact using SCAPS 1D simulator. American Journal of Optics and Photonics, 2019. 7(2): p. 33.
55. Dullweber, T., U. Rau, and H. Schock, A new approach to high-efficiency solar cells by band gap grading in Cu (In, Ga) Se2 chalcopyrite semiconductors. Solar Energy Materials and Solar Cells, 2001. 67(1-4): p. 145-150.
56. Fu, S., et al., Synergistic bimolecular erosion-healing interfacial passivation for wide-bandgap perovskite and tandem solar cells. Science Bulletin, 2025. 70(11): p. 1786-1792.
57. Chen, C., et al., High performance wide-bandgap perovskite solar cells based on bulk and top surface dual passivation. Chemical Engineering Journal, 2025: p. 169605.
58. Huang, Z., et al., Band engineering via gradient molecular dopants for CsFA perovskite solar cells. Advanced Functional Materials, 2021. 31(18): p. 2010572.
59. Hu, M., et al., Post-treatment of metal halide perovskites: from morphology control, defect passivation to band alignment and construction of heterostructures. Advanced Energy Materials, 2023. 13(41): p. 2301888.
60. Khorshidi, E., et al., Antisolvent additive engineering for boosting performance and stability of graded heterojunction perovskite solar cells using amide-functionalized graphene quantum dots. ACS applied materials & interfaces, 2022. 14(49): p. 54623-54634.
61. Wang, H., et al., Additive Engineering for mixed lead–tin narrow-band-gap perovskite solar cells: Recent advances and perspectives. Energy & Fuels, 2023. 37(9): p. 6401-6423.
62. Dixit, H., D. Punetha, and S.K. Pandey, Improvement in performance of lead free inverted perovskite solar cell by optimization of solar parameters. Optik, 2019. 179: p. 969-976.
63. Mandadapu, U., et al., Optimisation of high efficiency tin halide perovskite solar cells using SCAPS-1D. International journal of simulation and process modelling, 2018. 13(3): p. 221-227.
64. Mari, B. and K.R. Adhikari, Numerical Simulations on Perovskite Photovoltaic Devices. Chapters, 2016.
65. Singh, M., R. Kumar, and V. Singh, Graphene as charge transport layers in lead free perovskite solar cell. Materials Research Express, 2019. 6(11): p. 115611.
66. Cho, K.T., et al., Highly efficient perovskite solar cells with a compositionally engineered perovskite/hole transporting material interface. Energy & Environmental Science, 2017. 10(2): p. 621-627.
67. Bai, Y., et al., Dimensional engineering of a graded 3D–2D halide perovskite interface enables ultrahigh Voc enhanced stability in the p-i-n photovoltaics. Advanced Energy Materials, 2017. 7(20): p. 1701038.